



**HAL**  
open science

# Powder Metallurgy Processing and Characterization of the $\chi$ Phase Containing Multicomponent Al-Cr-Fe-Mn-Mo Alloy

Tomasz Stasiak, Mourtada-Aly Sow, Matthieu Touzin, Franck Béclin,  
Catherine Cordier

► **To cite this version:**

Tomasz Stasiak, Mourtada-Aly Sow, Matthieu Touzin, Franck Béclin, Catherine Cordier. Powder Metallurgy Processing and Characterization of the  $\chi$  Phase Containing Multicomponent Al-Cr-Fe-Mn-Mo Alloy. *Alloys*, 2023, *Alloys*, 2 (1), pp.44-54. 10.3390/alloys2010003 . hal-03991717

**HAL Id: hal-03991717**

**<https://hal.univ-lille.fr/hal-03991717v1>**

Submitted on 16 Feb 2023

**HAL** is a multi-disciplinary open access archive for the deposit and dissemination of scientific research documents, whether they are published or not. The documents may come from teaching and research institutions in France or abroad, or from public or private research centers.


L'archive ouverte pluridisciplinaire **HAL**, est destinée au dépôt et à la diffusion de documents scientifiques de niveau recherche, publiés ou non, émanant des établissements d'enseignement et de recherche français ou étrangers, des laboratoires publics ou privés.



Distributed under a Creative Commons Attribution 4.0 International License

## Article

# Powder Metallurgy Processing and Characterization of the $\chi$ Phase Containing Multicomponent Al-Cr-Fe-Mn-Mo Alloy

Tomasz Stasiak <sup>1,2,\*</sup> , Mourtada Aly Sow <sup>1</sup>, Matthieu Touzin <sup>1</sup>, Franck Béclin <sup>1</sup> and Catherine Cordier <sup>1</sup>

<sup>1</sup> Université de Lille, CNRS, INRAE, Centrale Lille, UMR 8207—UMET—Unité Matériaux et Transformations, F-59000 Lille, France

<sup>2</sup> National Centre for Nuclear Research, A. Soltana 7, PL-05-400 Otwock, Swierk, Poland

\* Correspondence: t.stasiak@yahoo.pl; Tel.: +48-510-443-296

**Abstract:** High entropy alloys present many promising properties, such as high hardness or thermal stability, and can be candidates for many applications. Powder metallurgy techniques enable the production of bulk alloys with fine microstructures. This study aimed to investigate powder metallurgy preparation, i.e., mechanical alloying and sintering, non-equiatomic high entropy alloy from the Al-Cr-Fe-Mn-Mo system. The structural and microstructural investigations were performed on powders and the bulk sample. The indentation was carried out on the bulk sample. The mechanically alloyed powder consists of two bcc phases, one of which is significantly predominant. The annealed powder and the sample sintered at 950 °C for 1 h consist of a predominantly bcc phase (71 ± 2 vol.%), an intermetallic  $\chi$  phase (26 ± 2 vol.%), and a small volume fraction of multielement carbides— $M_6C$  and  $M_{23}C_6$ . The presence of carbides results from carbon contamination from the balls and vial during mechanical alloying and the graphite die during sintering. The density of the sintered sample is 6.71 g/cm<sup>3</sup> (98.4% relative density). The alloy presents a very high hardness of 948 ± 34 HV<sub>1N</sub> and Young's modulus of 245 ± 8 GPa. This study showed the possibility of preparing ultra-hard multicomponent material reinforced by the intermetallic  $\chi$  phase. The research on this system presented new knowledge on phase formation in multicomponent systems. Moreover, strengthening the solid solution matrix via hard intermetallic phases could be interesting for many industrial applications.

**Keywords:** high entropy alloy; multicomponent material; compositionally complex alloy; powder metallurgy; mechanical alloying; sintering; phase structure; chi-phase



**Citation:** Stasiak, T.; Sow, M.A.; Touzin, M.; Béclin, F.; Cordier, C. Powder Metallurgy Processing and Characterization of the  $\chi$  Phase Containing Multicomponent Al-Cr-Fe-Mn-Mo Alloy. *Alloys* **2023**, *2*, 44–54. <https://doi.org/10.3390/alloys2010003>

Academic Editor:  
Konstantinos Georarakis

Received: 1 January 2023  
Revised: 24 January 2023  
Accepted: 8 February 2023  
Published: 13 February 2023



**Copyright:** © 2023 by the authors. Licensee MDPI, Basel, Switzerland. This article is an open access article distributed under the terms and conditions of the Creative Commons Attribution (CC BY) license (<https://creativecommons.org/licenses/by/4.0/>).

## 1. Introduction

High entropy alloys (HEAs), also known as compositionally complex alloys (CCAs), are multicomponent materials consisting of at least five main elements, each of them with content between 5 and 35 at.% [1]. The research on HEAs started with the introduction of CoCrFeMnNi alloy, known as Cantor alloy, showing promising properties [2]. However, nowadays, HEAs consist of different elements and can be divided into different groups, such as 3d-transition metal, 4f-transition metal, refractory metal, and light metal [3]. Moreover, some HEAs contain elements from different groups. HEAs present a very wide range of promising properties depending on the chemical composition, processing, and microstructure. HEAs are under current scientific interest from different fields of materials science [1,4,5]. The most common properties are high strength and ductility at high and low temperatures, high hardness, creep resistance, thermal stability, irradiation resistance, good weldability, oxidation resistance, resistance to corrosion, and hydrogen embrittlement [6]. Many exceptional properties of HEAs could be explained, at least partially, by their multielement composition, and the four core effects resulting from that, i.e., high entropy effect (solid solution stabilization), cocktail effect (unexpected synergies of properties of constituent elements), sluggish diffusion (thermal stability, easy formation of nanograin structure), and severe lattice distortion (high mechanical strength) [7]. However, in the

literature, there is debate on whether the four core effects are valid and could explain the aforementioned properties [8,9]. Many promising HEAs were developed and studied very recently. A good example could be  $\text{Al}_{0.25}\text{CoCrFeNiSi}_{0.6}$ , showing the structure of the fcc and bcc phases reinforced by  $\text{Cr}_3\text{Si}$  precipitates [10]. The alloy reveals very high hardness of up to 710  $\text{HV}_{0.3}$  and improved wear resistance compared to other alloys. Another HEA showing promising mechanical properties is  $\text{AlTiVCoNi}$  [11]. The alloy shows a relatively low density of approximately  $6.24 \text{ g cm}^{-3}$  and consists of the bcc phase and  $\text{L}_{21}$  phase. The alloy presents a high hardness of 689  $\text{HV}_{0.2}$  and good mechanical properties at high temperatures that can compete with superalloys. Beyond mechanical properties, some recently studied HEAs present high irradiation resistance. It is the case for  $\text{MoNbTaTi}$ ,  $\text{MoNbTaW}$ , and  $\text{MoNbTaTiW}$ , they each consist of a single bcc phase and present high hardness values between 420 and 550 HV [12].

Most HEAs are prepared by traditional liquid methods consisting of melting, mixing, and casting. Powder metallurgy (PM), especially mechanical alloying (MA) and sintering below melting temperature (usually between  $0.5 T_m$  and  $0.9 T_m$  [13]), which is a solid-state fabrication technique, enables the production of multicomponent materials with nanometric grains without segregation or loss of elements due to evaporation (large difference in melting temperatures between elements) [14,15]. MA of multicomponent alloys is performed in different types of mills, such as planetary, vibrational, attritor, or shaker rod mills [15]. Moreover, mechanical alloying, a non-equilibrium process, leads to enhanced solid solubility and the formation of metastable phases, which cannot be obtained by other techniques. The mechanically alloyed powders of multicomponent alloys are sintered by different methods, such as spark plasma sintering, hot isostatic pressing, and hot press sintering [14]. Despite not being the most common consolidation method of HEAs, hot press sintering presents many advantages, such as good control of sintering parameters or the simplicity of equipment. HEAs are consolidated mainly between 700 and 1000 °C under a pressure of 30–80 MPa in a graphite die. The duration of the process is usually between 1 and 2 h [14,15].

Most HEAs consist of solid solution phases, such as body-centered cubic (bcc) or face-centered cubic (fcc), due to their stabilization by high mixing entropy resulting from the multielement composition [1]. However, in some HEAs, intermetallic phases, such as Laves,  $\sigma$ ,  $\text{B}_2$ ,  $\text{L}_{12}$ ,  $\text{L}_{21}$ ,  $\mu$ ,  $\chi$ , and  $\eta$ , were detected [16]. The  $\sigma$  is the most commonly detected intermetallic phase in HEAs [17], but other intermetallics are less frequently reported. One of them is the  $\chi$  phase [18–23], which is detected more commonly in steels [24,25] and was first described by Andrews [26]. The  $\chi$  phase is based on the bcc structure (space group:  $\text{I-43m}$  (217)) with a large lattice parameter of 8.92 Å [24]. The hardness of the  $\chi$  phase in the  $\text{Al}_{0.25}\text{Ti}_{0.75}\text{CoCrFeNi}$  HEA is approximately 1090 HV [19]. Therefore, a hard intermetallic phase, such as  $\chi$  phase, could improve the hardness and wear resistance.

Among many investigated HEA systems, the Al-Cr-Fe-Mn-Mo family seems to present a promising structure and properties. Calculation by CALPHAD of the equiatomic AlCrFeMnMo alloy revealed that the structure at room temperature consists of two phases—bcc and  $\text{AlMo}_3$ —and its melting temperature is at 1600 °C [27]. The alloy shows a density of  $7.0 \text{ g/cm}^3$  and Young's modulus of 213 GPa. In addition, the choice of these elements could be explained as follows: Al to decrease density, Cr to increase corrosion resistance, Fe and Mn to reduce the cost, and Mo to improve hardness and high-temperature properties. Later, other papers on the promising Al-Cr-Fe-Mn-Mo family appeared [28–31]. Moreover, the experimental works on this family show the possibility of preparing mechanically alloyed powder consisting of two bcc phases [32]. The studies on the bulk samples revealed high hardness and high mechanical resistance under compression at high temperatures [33]. In addition, the investigation of the equiatomic AlCrFeMnMo alloy reveals the possibility of the formation of a high amount of carbides due to carbon contamination from stearic acid during mechanical alloying and the presence of two strong carbide former elements (Cr and Mo) [34]. Moreover, this multicomponent system was studied in the form of magnetron-sputtered thin films and showed encouraging results [35]. Therefore, it seems

interesting to continue the studies of different compositions from the Al-Cr-Fe-Mn-Mo family prepared by PM due to a large difference in melting temperature between elements.

In this study, the main aim was to prepare a novel non-equiatomic HEA with very high hardness. Compared to the equiatomic alloy, a lower content of Mo was selected to improve homogenization during mechanical alloying and decrease the density of the alloy, while a higher content of Fe was chosen to reduce the cost. A non-equiatomic alloy from the Al-Cr-Fe-Mn-Mo system was selected and prepared by powder metallurgy techniques. The investigation focused on the structure and microstructure of mechanically alloyed, annealed powders, and the sintered bulk sample. The main focus was on the presence of the  $\chi$  phase, which is very rarely reported in multicomponent alloys. Moreover, mechanical properties were evaluated by the indentation test. It should be noted that it is the first experimental study of this composition in bulk samples.

## 2. Materials and Methods

### 2.1. Material Preparation

The samples were prepared by PM techniques, i.e., MA and hot press sintering. The elemental powders were purchased from the company Goodfellow. The purity and particle sizes were as follows: Al (>99.0%, <15  $\mu\text{m}$ ), Cr (>99.0%, 38–45  $\mu\text{m}$ ), Fe (>99.0%, <60  $\mu\text{m}$ ), Mn (>99.5%, <45  $\mu\text{m}$ ), and Mo (>99.9%, <350  $\mu\text{m}$ ). The raw powders were mechanically alloyed in a vibrational mill SPEX 8000 operating at 18 Hz. The composition of the powder mixture before milling was as follows: 19 at.% Al, 22 at.% Cr, 34 at.% Fe, 19 at.% Mn, 6 at.% Mo. This corresponds to the composition of the bcc phase defined in a previous paper dealing with the Al-Cr-Fe-Mn-Mo family [33]. The parameters of MA were selected based on our previous articles [32,33]. The MA was conducted for 32 h at close to room temperature under an argon atmosphere using a vial and balls made of hardened steel. Breaks in milling were applied to prevent the heating of the powder—30 min break after each hour of milling. The ball–powder ratio was 10:1. The powders were mechanically alloyed without adding a process control agent because frontal shocks in a vibrational mill cause less agglomeration than shocks in a planetary mill. The alloyed powder was annealed at 950 °C for 1 h under argon in a high-temperature furnace (Centorr Vacuum Industries). Before the consolidation, the MA powder was put into 10 mm-diameter graphite die, which is common for such processing, to produce a sample of a height of 5 mm. For easier sample removal after sintering, graphite foils were placed between the punches, powder, and die. All manipulations with the powder were conducted in a glove box filled with argon to avoid powder oxidation. The sintering was carried out under argon at 950 °C for 1 h in a Centorr Vacuum Industries furnace equipped with an Instron 4507 press under a load of 80 MPa. The heating and cooling rates were 10 °C per minute.

### 2.2. Material Characterization

The phase information of the mechanically alloyed powder, annealed powder, and bulk sample was obtained from the X-ray diffraction (XRD) investigations using an X'PERT Pro Philips–Panalytical equipped with a cobalt tube ( $\lambda_{\text{K-alphaCo}} = 1.79021 \text{ \AA}$ ) working at 20 mA and 40 kV. Scans were acquired at a rate of 0.03 °/min in the range of 2 theta between 20° and 120°. The XRD data were analyzed using DIFFRAC.EVA software by Bruker and compared with the files of existing phases from the PDF ICDD database. Mössbauer spectrometry (MS) was conducted at room temperature using a  $^{57}\text{Co}$  (Rh) source and Aries-Wissel devices. Mössbauer spectra were deconvoluted using Lorentzian shape peaks and iron as reference. The following Mössbauer parameters were calculated: the peak width (W), hyperfine field (HF), quadrupole splitting (QS), isomer shift (IS), and relative amount of each iron environment (A). The scanning electron microscope (SEM) investigations were performed using a JEOL JSM-7800F with an energy-dispersive X-ray spectroscopy detector (EDX). The powder and bulk samples were prepared using a standard metallographic preparation method, i.e., hot mounting and polishing with grinding papers up to P4000. The final preparation was performed using diamond polishing pastes with a diamond size

of 3.0, 1.0, and 0.25  $\mu\text{m}$ . The volume fraction of phases in the annealed powder and the bulk sample was determined based on many SEM backscattered electrons (BSE) images using ImageJ software. The density measurements were performed according to Archimedes' principle in air and ethanol using a Mettler Toledo balance. The Vickers micro-hardness of the bulk sample was measured using a CSM Instruments Micro-Hardness Tester. For each load between 0.5 and 9 N, 15 measurements were performed at a dwell time of 10 s. The minimal space between indents was the distance of the five-time diameter of the biggest indent. Data were analyzed using the Oliver–Pharr method [36].

### 3. Results and Discussion

#### 3.1. Structure

According to the XRD results (Figure 1), the MA powder consists of two bcc phases. The predominant phase is bcc#2 ( $a = 2.91 \text{ \AA}$ , lattice parameter close to chromium and iron, ICDD PDF 00-006-0694), while the minor phase is bcc#1 ( $a = 3.13 \text{ \AA}$ , lattice parameter close to molybdenum, ICDD PDF 00-004-0809). Similar lattice parameters were detected in other powders from the Al–Cr–Fe–Mn–Mo system [32]. The formation of the bcc phase after MA is not surprising because Cr, Fe, Mn, and Mo present the bcc structure as pure elements, while Al is known as a bcc phase stabilizer. The annealing of the powder at 950  $^{\circ}\text{C}$  causes the disappearance of the bcc#1 phase. The annealed powder consists of a predominant bcc#2 phase ( $a = 2.90 \text{ \AA}$ ), intermetallic  $\chi$  phase ( $a = 8.95 \text{ \AA}$ ; space group: I-43m (217), ICDD PDF 01-081-3981), and very small fractions of carbides— $\text{M}_6\text{C}$  ( $a = 11.15 \text{ \AA}$ ; space group: Fd-3m (227), ICDD PDF 01-083-3017) and  $\text{M}_{23}\text{C}_6$  ( $a = 10.66 \text{ \AA}$ ; space group Fm-3m (225), ICDD PDF 00-035-0783). The structure of the bulk sample is similar to that of the annealed powder. The presence of carbides is related to the carbon contamination from balls and vial materials during MA and from graphite die during sintering. Carbon contamination during powder metallurgy processing is common and often results in the formation of carbides [14,15].

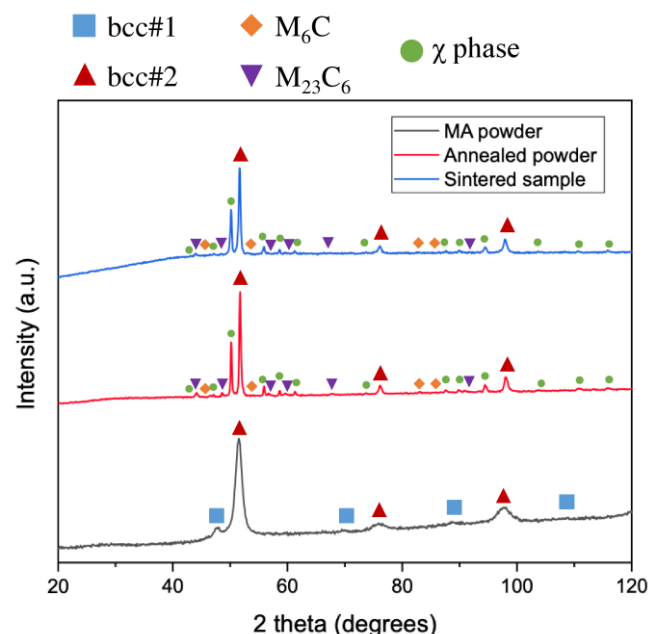


**Figure 1.** XRD patterns of MA powder, annealed powder, and sintered sample.

MS results revealed that the MA powder is more homogeneous than the annealed powder (Figure 2a,b, and Table 1), for which the acquired Mössbauer spectra are less symmetrical and broader. Moreover, the number of different iron sites increases after the heat treatment. It is the result of the multiphase structure of annealed powder (mostly bcc and  $\chi$  phases) compared to the largely predominant bcc#2 phase in MA powder.

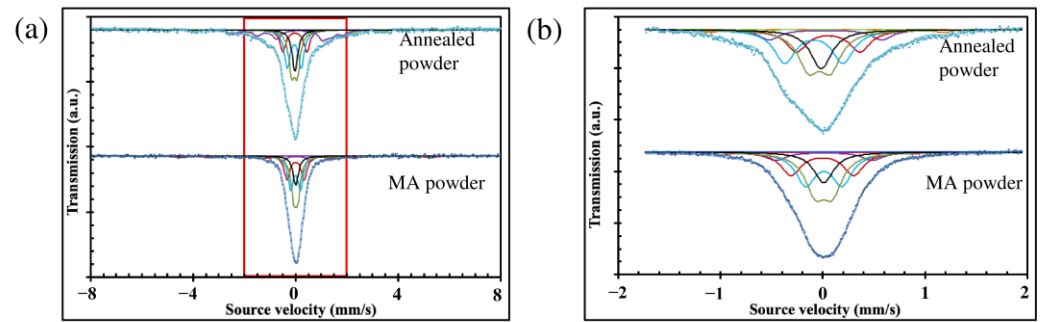


**Figure 2.** Mössbauer spectra of MA and annealed powder: (a) main spectra; (b) zoomed central part of the spectra.

**Table 1.** Mössbauer hyperfine parameters, such as the hyperfine field (H), isomer shift (IS), quadrupole splitting (QS), peak width (W), and relative amount of each iron environment (A) of iron environments in the mechanically alloyed powder and annealed powder.

Sample	Iron Site	H (T)	IS (mm/s)	QS (mm/s)	W (mm/s)	A (%)	Magnetic Properties
Annealed powder	Site 1	$33.6 \pm 1$	$0.03 \pm 0.08$	$0.28 \pm 0.08$	$0.32 \pm 0.08$	$5.75 \pm 0.65$	<b>Magnetic:</b> $29.82 \pm 1.79\%$ <b>Non-magnetic:</b> $70.18 \pm 1.79\%$
	Site 10	$13.5 \pm 1$	$-0.19 \pm 0.02$	$-0.12 \pm 0.02$	$0.34 \pm 0.09$	$17.60 \pm 1.02$	
	Site 11	-	$-0.08 \pm 0.11$	$1.46 \pm 0.36$	$0.29 \pm 0.04$	$6.47 \pm 0.12$	
	Site 5	-	$0.02 \pm 0.04$	$0.77 \pm 0.31$	$0.26 \pm 0.02$	$13.55 \pm 0.04$	
	Site 6	-	$-0.07 \pm 0.01$	$0.56 \pm 0.01$	$0.26 \pm 0.02$	$21.44 \pm 1.11$	
	Sites 9 + 12	-	$-0.04 \pm 0.01$	$0.21 \pm 0.01$	$0.26 \pm 0.01$	$22.91 \pm 0.47$	
	Site 8	-	$-0.02 \pm 0.01$	0	$0.26 \pm 0.01$	$12.28 \pm 0.02$	
MA powder	Sites 2 + 3	$30.5 \pm 1$	$-0.08 \pm 0.08$	$0.46 \pm 0.15$	$0.39 \pm 0.04$	$6.44 \pm 1.03$	<b>Magnetic:</b> $9.93 \pm 4.53\%$ <b>Non-magnetic:</b> $90.07 \pm 4.53\%$
	Sites 4 + 5	-	$0.02 \pm 0.01$	$1.02 \pm 0.08$	$0.26 \pm 0.03$	$5.94 \pm 1.05$	
	Site 6	-	$-0.01 \pm 0.01$	$0.64 \pm 0.03$	$0.25 \pm 0.02$	$19.48 \pm 0.86$	
	Site 7	-	$0.01 \pm 0.01$	$0.37 \pm 0.02$	$0.25 \pm 0.02$	$26.19 \pm 0.36$	
	Site 12	-	$0.01 \pm 0.01$	$0.16 \pm 0.02$	$0.25 \pm 0.02$	$29.61 \pm 0.04$	
	Site 8	-	$0.01 \pm 0.01$	0	$0.25 \pm 0.02$	$12.34 \pm 1.06$	

### 3.2. Microstructure

SEM secondary electron observations of MA powder showed the agglomeration of small particles with a very rugged surface (Figure 3a). The particles present a rather elongated shape. Most of the powder particles are of a size between 3 and 5  $\mu\text{m}$ . It should be noted that powder agglomeration occurs, even though the frontal shocks in a vibrational mill cause less agglomeration than shocks in a planetary mill. Some agglomerates are of a size of up to a few tens of micrometers. The process control agent could probably minimize the agglomeration; however, it will introduce contamination, mostly carbon, to the powder. The significant carbon contamination could lead to the formation of a high volume fraction of carbides and significantly change the phase formation during annealing or sintering, which was the case in other studies on the Al-Cr-Fe-Mn-Mo system [34]. Therefore, a process control agent was not added in this study.

The SEM microstructural analysis of MA powder was conducted to verify the homogeneity of the powder before sintering. The powder is homogeneous in the SEM-BSE images (Figure 3b), which means it is not possible to distinguish the bcc phases at this scale of analysis. It is related to a nanometric grain size which is common for powder metallurgy samples [13]. However, slight contamination by iron was detected by EDX, which is related to the erosion of the balls and vial during MA. The final composition is 18 at.% Al, 21 at.% Cr, 37 at.% Fe, 18 at.% Mn, 6 at.% Mo, close to the starting composition. The analysis of the annealed powder revealed a significantly different microstructure (Figure 3c). Nevertheless, the particle size and morphology of the annealed powder did not significantly change compared to mechanically alloyed powder. Based on the comparison between SEM, EDX, and XRD results, the dark grey matrix phase was associated with the bcc#2 and the light grey contrast corresponds to the intermetallic  $\chi$  phase. The grey contrast was associated

with  $M_{23}C_6$  carbide, while white spots correspond to  $M_6C$  carbide. The microstructure of the bulk sample (Figure 3d) is similar to that of the annealed powder. The analysis of the annealed powder and the bulk sample showed that the resulting structure is purely the effect of the temperature, and the pressure during sintering did not impact the phase formation. Moreover, it should be noted that the phases are distributed homogeneously, which confirms further uniform distribution of elements in MA powder. The MA process seems crucial in obtaining a homogeneous distribution of phases in the bulk sample.

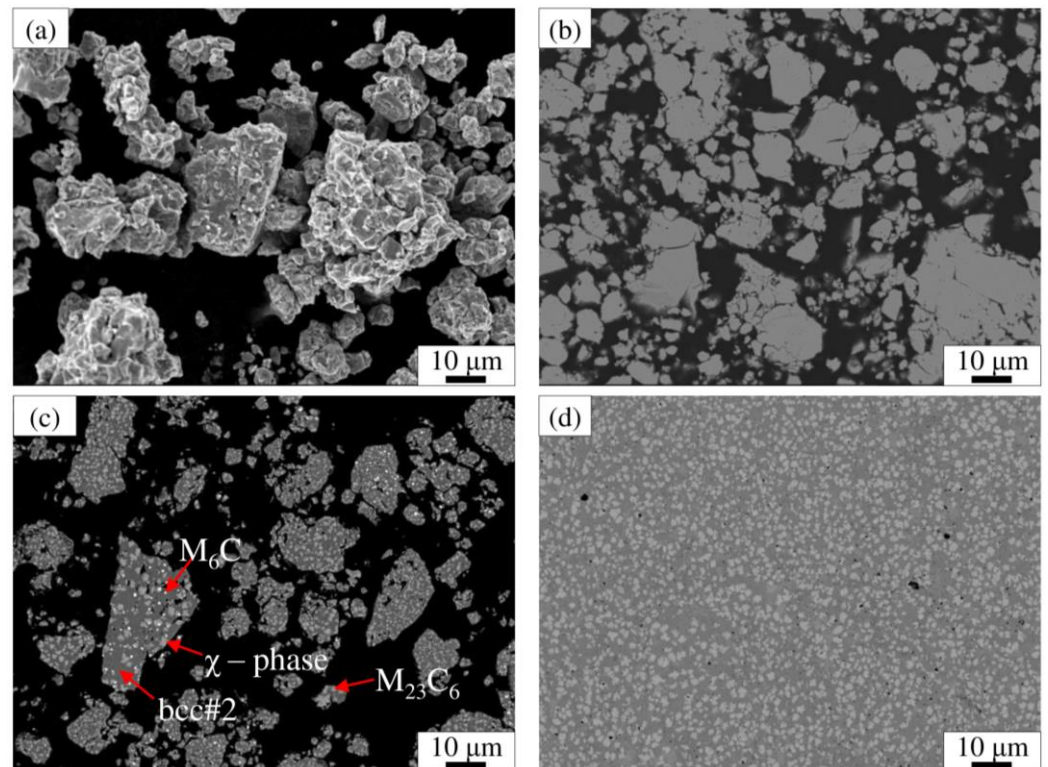


**Figure 3.** SEM images: (a) MA non-polished powder; (b) MA powder; (c) annealed powder; (d) sintered sample.

The SEM-EDX analyses (Figure 4 and Table 2) showed that the bcc phase has a composition relatively close to the overall powder composition, and the  $\chi$  phase is slightly enriched in Mo (approximately 11 at.%). The  $M_{23}C_6$  carbide is chromium-rich, while  $M_6C$  is rich in molybdenum, which is common for these carbides. The volume fraction of phases in the center of the sample (shown in Table 2) revealed a predominance of the bcc#2 phase and high content of the  $\chi$  phase. Some small volume fractions of carbides ( $M_6C$  and  $M_{23}C_6$ ) were also detected. The volume fraction of phase in annealed powder is similar to that of the bulk sample, i.e.,  $71 \pm 2\%$  of bcc#2 phase,  $27 \pm 2\%$  of  $\chi$  phase,  $1 \pm 1\%$  of  $M_6C$ , and  $1 \pm 1\%$  of  $M_{23}C_6$ . The results concerning phase content are in agreement with the XRD results, which revealed a predominance of bcc#2 phase, a high-volume fraction of  $\chi$  phase, and a small content of multielement carbides.

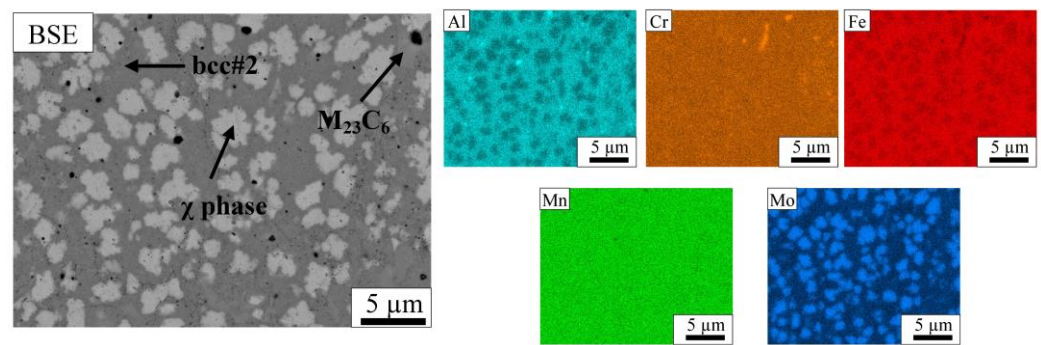


Figure 4. SEM-EDX mapping in the center of the bulk sample.

Table 2. Chemical composition (without quantifying light elements, such as carbon or oxygen) and volume fraction of phases in the center of the bulk sample.

Phase	Volume Fraction [%]	Atomic Concentration [at.%]				
		Al	Cr	Fe	Mn	Mo
bcc#2	71 ± 2	19.1	19.4	39.2	18.3	4.0
χ phase	26 ± 2	13.5	22.0	34.7	18.9	10.9
M <sub>6</sub> C	1 ± 1	13.1	15.6	24.2	10.8	36.3
M <sub>23</sub> C <sub>6</sub>	2 ± 1	4.3	55.5	17.0	14.2	9.0

The formation of multicomponent carbides is not surprising because similar carbides form in many HEAs prepared by powder metallurgy due to contamination by carbon in such processing from vial and ball materials and from graphite die during consolidation [14,15]. The contamination during MA is more homogeneously distributed, while the contamination during sintering is rather close to the surface of the sample. Similarly to this study, M<sub>6</sub>C is usually molybdenum-rich [37,38], while M<sub>23</sub>C<sub>6</sub> is usually chromium-rich [39–41] according to the literature. However, the formation of the rarely detected intermetallic χ phase is very surprising. The presence of the χ phase could be due to the significant presence of Fe, Cr, and Mo in the alloy, which favors the formation of this phase. In addition, it should be noted that in the literature, a close link between the χ phase and M<sub>6</sub>C carbide is noted. It seems that both phases can exist in equilibrium or substitute each other depending on the heat treatment performed [42]. It is worth mentioning that the χ phase is a part of the Cr-Fe-Mo ternary system [43] and, in high molybdenum stainless steels, can be described as Fe<sub>36</sub>Cr<sub>12</sub>Mo<sub>10</sub> according to Xu et al. [44]. In addition, from the structural point of view, the χ phase is considered to be an ordered α-Mn phase [21].

A different microstructure was detected in the area near the surface (a few tens of micrometers), which was in close contact with the graphite die during sintering (Figure 5). The significant contamination in this area due to the more pronounced diffusion of carbon from the graphite die led to a substantial decrease in the χ phase volume fraction and the formation of many M<sub>6</sub>C and M<sub>23</sub>C<sub>6</sub> carbides. The bcc#2 phase is still the predominant phase in this area. The formation of carbides needs significant amounts of molybdenum and chromium; therefore, the content of these elements seems to be insufficient to form the χ phase. Moreover, the carbon could dissolve (into the holes in the crystal structure) in the χ phase (sometimes classified as M<sub>18</sub>C), although in a significantly lower amount than in carbides [42]; thus, higher carbon contamination will favor the formation of carbides instead of the χ phase. In our previous study of a slightly different non-equiatomical chemical composition, the presence of the χ phase was not detected; however, the volume fraction of carbides seemed to be slightly higher [33]. Therefore, it could be concluded that very small changes in the content of elements, especially molybdenum, aluminum (bcc stabilizer), and carbon coming from contamination could significantly influence the phase formation in the investigated system. The density of the bulk sample is 6.71 g/cm<sup>3</sup>, which corresponds to 98.4% of the theoretical density calculated based on the density of pure elements. It



highlights the fact that the sintering parameters were correctly chosen to obtain a near-full-density bulk sample. Moreover, it shows that mechanical parameters were appropriately selected to not have internal porosity in powder particles. In addition, some agglomerates detected in mechanically alloyed powder did not significantly reduce the density of the bulk sample.

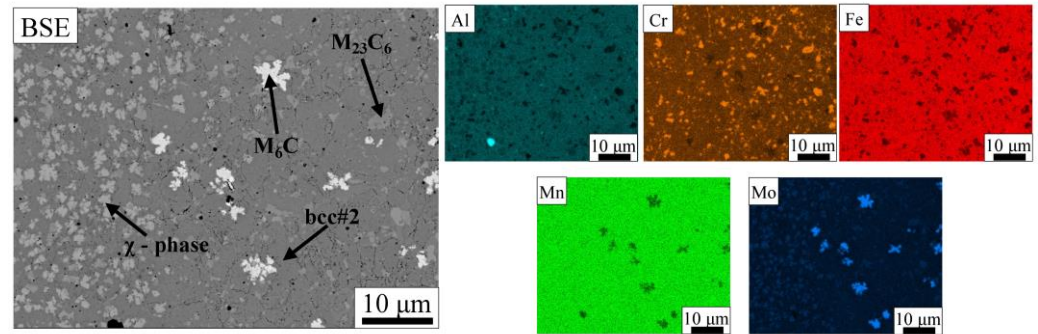


**Figure 5.** SEM-EDX mapping of the bulk sample of the area, which was in contact with the graphite die.

### 3.3. Mechanical Properties

The hardness of the bulk sample is very high, between 900 and 960 HV depending on the indentation load (Figure 6). A slight hardness decrease is observed with increasing load, which is related to the indentation size effect (ISE) [45]. The hardness is very high compared to other alloys prepared by powder metallurgy, e.g., 762 HV of AlCoCrFeNiTi<sub>0.5</sub> consisting of fcc, B2, sigma, and TiC phases [46] or 670 HV of AlCoCrFeNi consisting of a mixture of fcc and bcc phases [47]. The high hardness of the alloy could be beneficial in tribological and high wear-resistant applications. The high hardness is the effect of different strengthening mechanisms, such as solid solution strengthening (matrix bcc multielement solid solution), strengthening by very hard intermetallic phase ( $\chi$  phase), and grain boundary strengthening (fine grain size, in order between 200 and 400 nm based on our previous studies on this system [33]). The hardness of the  $\chi$  phase measured by Gwalani et al. [19] was 1090 HV  $\pm$  14; therefore, it is obvious that the  $\chi$  phase has an impact on the hardness of the produced sample. It should be noted that the  $\chi$  phase is harder than many other intermetallic phases, e.g., a Huesler phase with L2<sub>1</sub> ordering in studies by Gwalani et al. [19] or Laves phase in studies by Zhao et al. [18]. The bulk sample also presents a very high Young's modulus, e.g., 245  $\pm$  8 GPa for the measurement under a load of 1 N. The value is higher than the value of 213 GPa predicted by CALPHAD simulation of equiatomic AlCrFeMnMo alloy consisting of a bcc phase and AlMo<sub>3</sub> compound.

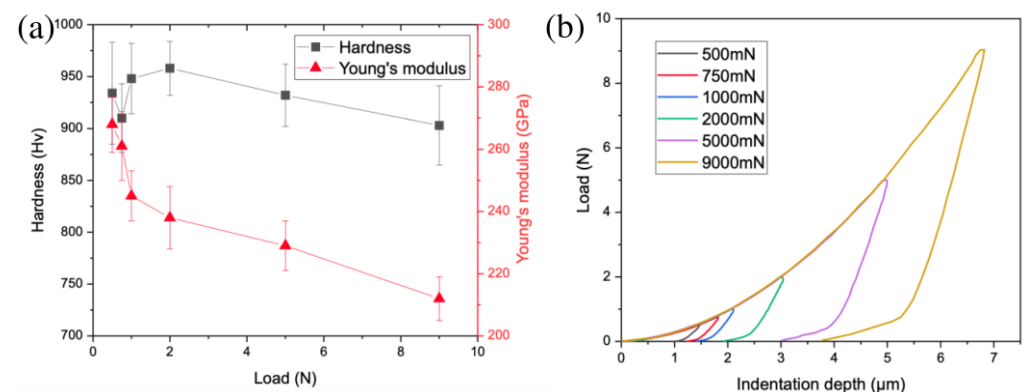


**Figure 6.** Mechanical properties investigations: (a) hardness and Young's modulus as a function of indentation load; (b) indentation curves under different loads.

The SEM observations revealed the presence of circumferential cracks in the vicinity of indentation sites (Figure 7). It shows the brittleness of the alloy, which is caused primarily

by the presence of the intermetallic  $\chi$  phase, which is known to be very brittle [48]. The brittleness increase due to the  $\chi$  phase was reported in other HEAs [18,19]. However, there are no radial cracks, which are typical for brittle material [49]. Therefore, some plasticity of this sample due to the less brittle matrix bcc phase is revealed.

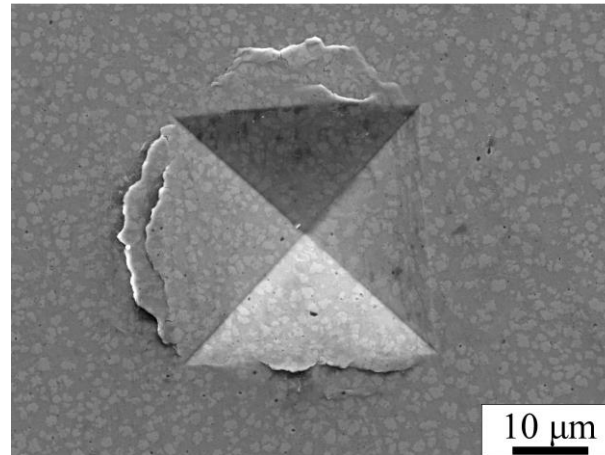


**Figure 7.** SEM secondary electron image of the indentation site showing circumferential cracks without the presence of radial cracks.

#### 4. Conclusions

Non-equiatomic HEA from the Al-Cr-Fe-Mn-Mo family was successfully prepared via powder metallurgy. The mechanically alloyed powder consists of two bcc phases. Annealing at 950 °C for 1 h led to the phase transformations. As a result, it was determined that the powder consists of a predominant bcc phase ( $71 \pm 2\%$ ), intermetallic  $\chi$  phase ( $27 \pm 2\%$ ), and small volume fraction ( $1 \pm 1\%$ ) of  $M_6C$  and  $M_{23}C_6$ . The bulk sample presents a similar microstructure with a higher volume fraction of carbides in the area close to the surface due to the diffusion of carbon from the graphite die during sintering. The main finding of this paper is the presence of the  $\chi$  phase in the bcc matrix in the multicomponent alloy. The intermetallic  $\chi$  phase is very rarely reported in HEA, but it can significantly improve the hardness. It can open new perspectives on research into multicomponent alloys with a hard  $\chi$  phase. The very high hardness and Young's modulus of the investigated bulk sample  $948 \pm 34$  HV<sub>1N</sub> and  $245 \pm 8$  GPa, respectively, show the need to investigate this HEA system further. Future studies should focus on the investigation of the wear resistance of HEA containing a high-volume fraction of the  $\chi$  phase. Moreover, the mechanisms behind the formation of the  $\chi$  phase in multicomponent alloys need to be better understood.

**Author Contributions:** Conceptualization, T.S., M.T., F.B. and C.C.; methodology, T.S., M.T., F.B. and C.C.; validation, T.S., M.A.S. and C.C.; formal analysis, T.S., M.A.S. and C.C.; investigation, T.S., M.A.S. and C.C.; resources, M.T. and F.B.; data curation, T.S. and C.C.; writing—original draft preparation, T.S.; writing—review and editing, M.T., F.B. and C.C.; visualization, T.S.; supervision, C.C.; project administration, C.C.; funding acquisition, C.C. All authors have read and agreed to the published version of the manuscript.

**Funding:** The author T.S. sincerely thanks the University of Lille and the Region “Hauts-de-France” for financially supporting his graduate doctoral program. The SEM and TEM national facility in Lille (France) is financially supported by the Region “Hauts-de-France”, the European Regional Development Fund (ERDF).

**Data Availability Statement:** The data presented in this study are available on request from the corresponding author.

**Acknowledgments:** Damien Creton is acknowledged for his assistance in the sample preparation.

**Conflicts of Interest:** The authors declare no conflict of interest. The funders had no role in the design of the study; in the collection, analyses, or interpretation of data; in the writing of the manuscript; or in the decision to publish the results.

## References

1. George, E.P.; Raabe, D.; Ritchie, R.O. High-Entropy Alloys. *Nat. Rev. Mater.* **2019**, *4*, 515–534. [[CrossRef](#)]
2. Cantor, B.; Chang, I.T.H.; Knight, P.; Vincent, A.J.B. Microstructural Development in Equiatomic Multicomponent Alloys. *Mater. Sci. Eng. A* **2004**, *375–377*, 213–218. [[CrossRef](#)]
3. Gorsse, S.; Miracle, D.B.; Senkov, O.N. Mapping the World of Complex Concentrated Alloys. *Acta Mater.* **2017**, *135*, 177–187. [[CrossRef](#)]
4. Muhammad Nadzri, N.I.; Halin, D.S.C.; Al Bakri Abdullah, M.M.; Joseph, S.; Mohd Salleh, M.A.A.; Vizureanu, P.; Burduhos-Nergis, D.P.; Sandu, A.V. High-Entropy Alloy for Thin Film Application: A Review. *Coatings* **2022**, *12*, 1842. [[CrossRef](#)]
5. Gonçalves De Oliveira, T.; Fagundes, D.V.; Capellato, P.; Sachs, D.; Augusto, A.; Pinto Da Silva, A. A Review of Biomaterials Based on High-Entropy Alloys. *Metals* **2022**, *12*, 1940. [[CrossRef](#)]
6. Gao, M.C.; Liaw, P.K.; Yeh, J.W.; Zhang, Y. *High-Entropy Alloys: Fundamentals and Applications*; Springer International Publishing: Berlin/Heidelberg, Germany, 2016; ISBN 9783319270135.
7. Yeh, J.-W. Recent Progress in High Entropy Alloys. *Ann. Chim.—Sci. Matériaux* **2006**, *31*, 633–648. [[CrossRef](#)]
8. Miracle, D.B.; Senkov, O.N. A Critical Review of High Entropy Alloys and Related Concepts. *Acta Mater.* **2017**, *122*, 448–511. [[CrossRef](#)]
9. Dąbrowa, J.; Zajusz, M.; Kucza, W.; Cieślak, G.; Berent, K.; Czeppe, T.; Kulik, T.; Danielewski, M. Demystifying the Sluggish Diffusion Effect in High Entropy Alloys. *J. Alloys Compd.* **2019**, *783*, 193–207. [[CrossRef](#)]
10. Samoilova, O.; Shaburova, N.; Ostovari Moghaddam, A.; Trofimov, E. Al<sub>0.25</sub>CoCrFeNiSi<sub>0.6</sub> High Entropy Alloy with High Hardness and Improved Wear Resistance. *Mater. Lett.* **2022**, *328*, 133190. [[CrossRef](#)]
11. Li, Y.; Liao, W.B.; Chen, H.; Brechtel, J.; Song, W.; Yin, W.; He, Z.; Liaw, P.K.; Zhang, Y. A Low-Density High-Entropy Dual-Phase Alloy with Hierarchical Structure and Exceptional Specific Yield Strength. *Sci. China Mater.* **2022**, *66*, 780–792. [[CrossRef](#)]
12. Zong, Y.; Hashimoto, N.; Oka, H. Study on Irradiation Effects of Refractory Bcc High-Entropy Alloy. *Nucl. Mater. Energy* **2022**, *31*, 101158. [[CrossRef](#)]
13. Sherif El-Eskandarany, M. *Mechanical Alloying*; Elsevier: Amsterdam, The Netherlands, 2015; ISBN 9781455777525.
14. Torralba, J.M.; Alvaredo, P.; García-Junceda, A. High-Entropy Alloys Fabricated via Powder Metallurgy. A Critical Review. *Powder Metall.* **2019**, *62*, 84–114. [[CrossRef](#)]
15. Vaidya, M.; Muralikrishna, G.M.; Murty, B.S. High-Entropy Alloys by Mechanical Alloying: A Review. *J. Mater. Res.* **2019**, *34*, 664–686. [[CrossRef](#)]
16. Tsai, M.H.; Tsai, R.C.; Chang, T.; Huang, W.F. Intermetallic Phases in High-Entropy Alloys: Statistical Analysis of Their Prevalence and Structural Inheritance. *Metals* **2019**, *9*, 247. [[CrossRef](#)]
17. Tsai, M.H.; Chang, K.C.; Li, J.H.; Tsai, R.C.; Cheng, A.H. A Second Criterion for Sigma Phase Formation in High-Entropy Alloys. *Mater. Res. Lett.* **2015**, *4*, 90–95. [[CrossRef](#)]
18. Zhao, Y.; Lau, K.B.; Teh, W.H.; Lee, J.J.; Wei, F.; Lin, M.; Wang, P.; Tan, C.C.; Ramamurty, U. Compositionally Graded CoCrFeNiTi<sub>x</sub> High-Entropy Alloys Manufactured by Laser Powder Bed Fusion: A Combinatorial Assessment. *J. Alloys Compd.* **2021**, *883*, 160825. [[CrossRef](#)]
19. Gwalani, B.; Ayyagari, A.V.; Choudhuri, D.; Scharf, T.; Mukherjee, S.; Gibson, M.; Banerjee, R. Microstructure and Wear Resistance of an Intermetallic-Based Al<sub>0.25</sub>Ti<sub>0.75</sub>CoCrFeNi High Entropy Alloy. *Mater. Chem. Phys.* **2018**, *210*, 197–206. [[CrossRef](#)]
20. Tsai, M.H.; Fan, A.C.; Wang, H.A. Effect of Atomic Size Difference on the Type of Major Intermetallic Phase in Arc-Melted CoCrFeNi<sub>x</sub> High-Entropy Alloys. *J. Alloys Compd.* **2017**, *695*, 1479–1487. [[CrossRef](#)]
21. Zendejas Medina, L.; Riekehr, L.; Jansson, U. Phase Formation in Magnetron Sputtered CrMnFeCoNi High Entropy Alloy. *Surf. Coatings Technol.* **2020**, *403*, 126323. [[CrossRef](#)]
22. Zendejas Medina, L.; Tavares da Costa, M.V.; Paschalidou, E.M.; Lindwall, G.; Riekehr, L.; Korvela, M.; Fritze, S.; Kolozsvári, S.; Gamstedt, E.K.; Nyholm, L.; et al. Enhancing Corrosion Resistance, Hardness, and Crack Resistance in Magnetron Sputtered High Entropy CoCrFeMnNi Coatings by Adding Carbon. *Mater. Des.* **2021**, *205*, 109711. [[CrossRef](#)]
23. Li, Y.; Hu, Y.; Zhang, D.; Cong, W. Laser Remelting of CoCrFeNiTi High Entropy Alloy Coatings Fabricated by Directed Energy Deposition: Effects of Remelting Laser Power. *Opt. Laser Technol.* **2023**, *158*, 108871. [[CrossRef](#)]
24. Lu, H.H.; Guo, H.K.; Luo, Y.; Liu, Z.G.; Li, W.Q.; Li, J.C.; Liang, W. Microstructural Evolution, Precipitation and Mechanical Properties of Hot Rolled 27Cr-4Mo-2Ni Ferritic Steel during 800 °C Aging. *Mater. Des.* **2018**, *160*, 999–1009. [[CrossRef](#)]
25. Lu, H.H.; Luo, Y.; Guo, H.K.; Li, W.Q.; Li, J.C.; Liang, W. Microstructural Evolution and Mechanical Properties of 27Cr-4Mo-2Ni Ferritic Stainless Steel during Isothermal Aging. *Mater. Sci. Eng. A* **2018**, *735*, 31–39. [[CrossRef](#)]
26. Andrews, K.W. A New Intermetallic Phase in Alloy Steels. *Nature* **1949**, *164*, 1015. [[CrossRef](#)]
27. Senkov, O.N.; Miller, J.D.; Miracle, D.B.; Woodward, C. Accelerated Exploration of Multi-Principal Element Alloys for Structural Applications. *Calphad Comput. Coupling Phase Diagr. Thermochem.* **2015**, *50*, 32–48. [[CrossRef](#)]
28. Besson, R. Understanding Phase Equilibria in High-Entropy Alloys: I. Chemical Potentials in Concentrated Solid Solutions—Atomic-Scale Investigation of AlCrFeMnMo. *J. Alloys Compd.* **2021**, *872*, 159745. [[CrossRef](#)]

29. Besson, R. Understanding Phase Equilibria in High-Entropy Alloys: II. Atomic-Scale Study of Incorporation of Metallic Elements in Cr Carbides—Application to Equilibrium with AlCrFeMnMo. *J. Alloys Compd.* **2021**, *874*, 159959. [[CrossRef](#)]
30. Besson, R. Ordering and Phase Separation in Multi-Principal-Element Metallic Alloys: Contribution from Mean-Field Atomic-Scale Modelling and Simulation. *J. Alloys Compd.* **2022**, *898*, 162842. [[CrossRef](#)]
31. Sekkal, W.; Besson, R.; Legris, A. Atomic Scale Modeling of Structural Phase Transformations in AlCrFeMnMo High-Entropy Alloys during Thermal Treatments. *J. Alloys Compd.* **2021**, *876*, 160201. [[CrossRef](#)]
32. Stasiak, T.; Kumaran, S.N.; Touzin, M.; Béclin, F.; Cordier, C. Novel Multicomponent Powders from the AlCrFeMnMo Family Synthesized by Mechanical Alloying. *Adv. Eng. Mater.* **2019**, *21*, 1900808. [[CrossRef](#)]
33. Stasiak, T.; Aly Sow, M.; Addad, A.; Touzin, M.; Bé Clin, F.; Cordier, C. Processing and Characterization of a Mechanically Alloyed and Hot Press Sintered High Entropy Alloy from the Al-Cr-Fe-Mn-Mo Family. *JOM* **2022**, *74*, 971–980. [[CrossRef](#)]
34. Stasiak, T.; Sow, M.A.; Touzin, M.; Béclin, F.; Cordier, C. Preparation and Characterisation of the Al-Cr-Fe-Mn-Mo High-Entropy Alloy Reinforced by in-Situ Formed Carbides. *Philos. Mag. Lett.* **2022**, *102*, 368–377. [[CrossRef](#)]
35. Santana, Y.Y.; Sow, M.A.; Nouvellon, C.; Cordier, C.; Beclin, F.; Touzin, M.; Tromont, A.; Noirfalise, X.; Boilet, L.; Trelcat, J.F.; et al. Influence of Powder Mixing Method on Properties of High Entropy Alloys of FeCrMnAlMo Thin Coatings Obtained by Magnetron Sputtering. *Surf. Coatings Technol.* **2022**, *446*, 128744. [[CrossRef](#)]
36. Oliver, W.C.; Pharr, G.M. An Improved Technique for Determining Hardness and Elastic Modulus Using Load and Displacement Sensing Indentation Experiments. *J. Mater. Res.* **1992**, *7*, 1564–1583. [[CrossRef](#)]
37. Sun, C.; Li, P.; Xi, S.; Zhou, Y.; Li, S.; Yang, X. A New Type of High Entropy Alloy Composite Fe<sub>18</sub>Ni<sub>23</sub>Co<sub>25</sub>Cr<sub>21</sub>Mo<sub>8</sub>WNb<sub>3</sub>C<sub>2</sub> Prepared by Mechanical Alloying and Hot Pressing Sintering. *Mater. Sci. Eng. A* **2018**, *728*, 144–150. [[CrossRef](#)]
38. Praveen, S.; Murty, B.S.; Kottada, R.S. Effect of Molybdenum and Niobium on the Phase Formation and Hardness of Nanocrystalline CoCrFeNi High Entropy Alloys. *J. Nanosci. Nanotechnol.* **2014**, *14*, 8106–8109. [[CrossRef](#)]
39. Praveen, S.; Anupam, A.; Tilak, R.; Kottada, R.S. Phase Evolution and Thermal Stability of AlCoCrFe High Entropy Alloy with Carbon as Unsolicited Addition from Milling Media. *Mater. Chem. Phys.* **2018**, *210*, 57–61. [[CrossRef](#)]
40. Xie, Y.; Zhou, D.; Luo, Y.; Xia, T.; Zeng, W.; Li, C.; Wang, J.; Liang, J.; Zhang, D. Fabrication of CoCrFeNiMn High Entropy Alloy Matrix Composites by Thermomechanical Consolidation of a Mechanically Milled Powder. *Mater. Charact.* **2019**, *148*, 307–316. [[CrossRef](#)]
41. Cheng, H.; Xie, Y.C.; Tang, Q.H.; Rao, C.; Dai, P.Q. Microstructure and Mechanical Properties of FeCoCrNiMn High-Entropy Alloy Produced by Mechanical Alloying and Vacuum Hot Pressing Sintering. *Trans. Nonferrous Met. Soc. China (Engl. Ed.)* **2018**, *28*, 1360–1367. [[CrossRef](#)]
42. Gavriljuk, V.G.; Berns, H. *High Nitrogen Steels: Structure, Properties, Manufacture, Applications*; Springer: Berlin/Heidelberg, Germany, 1999.
43. Llorca-Isern, N.; López-Luque, H.; López-Jiménez, I.; Biezma, M.V. Identification of Sigma and Chi Phases in Duplex Stainless Steels. *Mater. Charact.* **2016**, *112*, 20–29. [[CrossRef](#)]
44. Xu, W.; San Martin, D.; Rivera Díaz del Castillo, P.E.J.; van der Zwaag, S. Modelling and Characterization of Chi-Phase Grain Boundary Precipitation during Aging of Fe-Cr-Ni-Mo Stainless Steel. *Mater. Sci. Eng. A* **2007**, *467*, 24–32. [[CrossRef](#)]
45. Gong, J.; Li, Y. Energy-Balance Analysis for the Size Effect in Low-Load Hardness Testing. *J. Mater. Sci.* **2000**, *35*, 209–213. [[CrossRef](#)]
46. Moravcik, I.; Cizek, J.; Gavendova, P.; Sheikh, S.; Guo, S.; Dlouhy, I. Effect of Heat Treatment on Microstructure and Mechanical Properties of Spark Plasma Sintered AlCoCrFeNiTi<sub>0.5</sub> High Entropy Alloy. *Mater. Lett.* **2016**, *174*, 53–56. [[CrossRef](#)]
47. Fourmont, A.; Le Gallet, S.; Politano, O.; Desgranges, C.; Baras, F. Effects of Planetary Ball Milling on AlCoCrFeNi High Entropy Alloys Prepared by Spark Plasma Sintering: Experiments and Molecular Dynamics Study. *J. Alloys Compd.* **2020**, *820*, 153448. [[CrossRef](#)]
48. Duarte, M.J.; Kostka, A.; Jimenez, J.A.; Choi, P.; Klemm, J.; Crespo, D.; Raabe, D.; Renner, F.U. Crystallization, Phase Evolution and Corrosion of Fe-Based Metallic Glasses: An Atomic-Scale Structural and Chemical Characterization Study. *Acta Mater.* **2014**, *71*, 20–30. [[CrossRef](#)]
49. Dobrzański, L.; Dołżańska, B. Hardness to Toughness Relationship on WC-Co Tool Gradient Materials Evaluated by Palmqvist Method. *Arch. Mater. Sci. Eng.* **2010**, *43*, 87–93.

**Disclaimer/Publisher's Note:** The statements, opinions and data contained in all publications are solely those of the individual author(s) and contributor(s) and not of MDPI and/or the editor(s). MDPI and/or the editor(s) disclaim responsibility for any injury to people or property resulting from any ideas, methods, instructions or products referred to in the content.